Acoustic emission monitoring of composite marine propellers in submerged conditions using embedded piezoelectric sensors

Huijer, A.J.; Kassapoglou, C.; Pahlavan, Lotfollah

DOI
10.1088/1361-665X/ad6739

Publication date
2024

Document Version
Final published version

Published in
Smart Materials and Structures

PAPER • **OPEN ACCESS**

Acoustic emission monitoring of composite marine propellers in submerged conditions using embedded piezoelectric sensors

To cite this article: Arnaud Huijer *et al* 2024 *Smart Mater. Struct.* **33** 095018

OPEN ACCESS
IOP Publishing
Smart Materials and Structures
Smart Mater. Struct. **33** (2024) 095018 (10pp)
https://doi.org/10.1088/1361-665X/ad6739

Acoustic emission monitoring of composite marine propellers in submerged conditions using embedded piezoelectric sensors

Arnaud Huijer[1,*], **Christos Kassapoglou**[2] **and Lotfollah Pahlavan**[1]

[1] Faculty of Mechanical Engineering, Delft University of Technology, Delft, The Netherlands
[2] Faculty of Aerospace Engineering, Delft University of Technology, Delft, The Netherlands

E-mail: a.j.huijer@tudelft.nl

Received 7 March 2024, revised 27 June 2024
Accepted for publication 24 July 2024
Published 8 August 2024

Abstract

Flexible composite marine propellers can aid the marine industry in reducing carbon emissions and underwater radiated noise pollution. The structural integrity of the blades can be assessed using structural health monitoring. One of these methods is the measurement and analysis of damage-induced acoustic emission signals. This paper experimentally investigates the feasibility of using embedded piezoelectric sensors for the measurement of acoustic emissions throughout a submerged flexible composite marine propeller blade. A full-scale glass-fibre reinforced polymer blade has been manufactured with 24 embedded sensors. While suspended in artificial seawater, acoustic emissions were simulated on the blade. The measurements show that the embedded piezoelectric sensors can measure acoustic emissions while the blade is submerged. Further, the distance from source to sensor over which the acoustic emission is measurable was investigated. For a noise level of 40 dB and a source amplitude of 70 dB between 100 and 250 kHz, an average maximum measurable distance of 124 mm was obtained. For higher frequencies, the distance drops and for lower noise levels the distance increases.

Keywords: acoustic emission, embedded sensor, composite marine propeller, piezoelectric sensor, damage detection

1. Introduction

The marine industry is in the process of improving its environmental footprint. This involves reduction of carbon emissions as well as reduction of underwater radiated noise (URN) for the protection of marine mammals [1, 2]. The use of flexible composite marine propellers is envisioned to help in obtaining these reductions. The directed flexibility of such propellers enables the blade shape to be adaptable to different loading conditions [3, 4]. This can improve efficiency [5]. Furthermore, pressure peaks on the blade are reduced due to blade-tip flexibility. This can lead to reduced URN [6]. Additional advantages of composite propeller blades are a reduced electromagnetic signature, lower weight, and the ability to have sensors incorporated [7].

The development of flexible composite marine propeller blades has encountered uncertainty regarding their behaviour in fatigue and failure. This matters as unanticipated failure of a propeller blade will considerably limit a vessel's manoeuvrability. Prominent causes to the uncertainty are deviations and imperfections during fabrication, the varying loading of

* Author to whom any correspondence should be addressed.

the blade, and a complex internal stress state imposed by the thick intricate geometry and spatially-varying material layup [8, 9]. Additionally, depending on their location and load history, different damage types may grow to gross failure or cause a stress redistribution that leads to different failure [10]. Given the complexities and the involved risk, there is a need for structural health monitoring (SHM) of flexible composite propeller blades.

In an advanced state of damage, the changes in material properties lead to global effects, such as an increased deformation or changes in vibrational response. This could be measured using externally mounted measurement devices such as cameras and hydrophones. Deformation behaviour of full-scale flexible propeller blades was measured *in-situ* by Maljaars *et al* [11] using digital image correlation (DIC). The cameras were installed on a ship rudder. Blade deformations were successfully captured, albeit hindered by underwater disturbances. The DIC method was similarly used in a cavitation tunnel for flexible propeller blades by Su *et al* [12]. Using laser beam irradiation and an image registration method, Shiraishi *et al* [13] were able to estimate the full-blade deformation shape of a flexible propeller in a cavitation tunnel. Kluczyk *et al* [14] described damage identification in flexible propeller blades by monitoring of hydroacoustic behaviour using hull-mounted hydrophones.

Sensors mounted onto or embedded into the blade can be used for the same purpose. There is a strong incentive to have the sensors embedded into the composite laminate. The blades are subject to harsh loading and environmental conditions, which would pose great challenges for surface-mounted sensors. Furthermore, surface-mounted sensors can obstruct the hydrodynamic performance of the blade. Investigations relating to composite hydrofoils include the use of embedded strain gauges, fibre-Bragg gratings (FBGs) and distributed optical fibres for strain measurements and accelerometers and piezoelectric sensors for modal assessments. Strain gauges were placed on flexible and metal model propeller blades by Tian *et al* [15]. They were able to measure vibratory responses. Zetterlind *et al* [16] compared the use of surface-mounted strain gauges and fibre-optic sensors for strain monitoring during fatigue assessment of composite aerospace propeller blades. The research described increased survivability of fibre-optic sensors compared to strain gauges. For a composite marine propeller blade, Seaver *et al* [17], embedded FBGs during manufacturing and demonstrated the feasibility of measuring strains in a water tunnel. Complexities were noted regarding the embedding procedure. FBGs were also used by Javdani *et al* [18], who placed these on the surface of a full-scale metal propeller. Modal analysis with the propeller submerged showed a good agreement with simulated results. Ding *et al* [19] measured strains on a model of a propeller blade using surface-mounted FBGs. Reconstructed deformations of the blade were created using an inverse finite element method. Error between reconstructions and deformation measurements was below 7%. Maung *et al* [20] embedded distributed optical fibres into a carbon-fibre composite hydrofoil. It was noted that the measured strains were in reasonable accordance with simulations. This research was continued by Shamsuddoha *et al* [8] who embedded distributed optical fibres into a full-scale composite hydrofoil loaded under fatigue. In that work, also piezoelectric accelerometers were placed to perform modal analysis. No notable change in modal properties was measured during the fatigue loading. The feasibility of using embedded piezoelectric sensors for the use of dynamic strain measurement of composite marine propeller blades was assessed by the authors from finite element simulations and small-scale experiments [21]. Hamada *et al* [22] placed piezoelectric line sensors on flexible propeller blades and tested them in operation. Changes in the vibration response of the propeller blade were measured for detection of damaged blades.

In early stages of damage the global effects become less pronounced and other methods for SHM in composite propellers become relevant. One promising method is the measurement and processing of acoustic emissions (AE). An AE signal is an ultrasound elastic burst emanating from material degradation. Fibre-reinforced composite materials have a multitude of damage mechanisms such as matrix cracking, fibre-matrix interface debonding, fibre breakage and fibre pull-out. Each of these mechanisms have distinct AE characteristics, such as specific frequency content and amplitude [23–25]. Conventionally, AE has been measured using piezoelectric sensors. These sensors allow for a high enough sample rate for measuring AE. Additionally, they can be miniaturized and embedded into various structures, including fibre-reinforced composites [25, 26] and concrete [27, 28].

In marine applications, simulated AE signals have previously been measured on a submerged steel half rudder blade. Measurement and localisation of an AE source was performed while comparing different sensor types [29]. Furthermore, AE investigations on composite tidal turbine blades are emerging [30]. Next to a preliminary feasibility study by the authors [21], no published research on AE in full-scale composite marine propeller blades is known to date.

The localisation of the AE ([31, 32]) and the characterisation of the damage mechanism can be fundamental in the assessment of the structural health and in the estimation of remaining lifetime of the structure. To enable localisation and characterisation, the measured signals need to be of sufficient signal to noise ratio. The evaluation for the signal to noise ratio requires estimations of the expected noise level and the AE source signal amplitude, and indication of the location of the degradation with respect to the sensor location. Further, the knowledge of the attenuation behaviour of AE for different degradation mechanisms is instrumental for this assessment.

Hence, wave propagation attenuation will influence the quality of the measured signal and the maximum measurable distance between a sensor and an AE source. This implies that wave propagation attenuation over the blade is of profound relevance for the assessment of the feasibility of localisation and characterisation of AE.

This paper investigates the measurement and attenuation of AE signals in a submerged composite marine propeller blade using embedded piezoelectric sensors. The research is believed to be the first reported investigation on the topic demonstrating AE measurement in an underwater composite

marine propeller blade using a network of embedded piezoelectric sensors.

The paper encompasses the experimental excitation, measurement and assessment of AE signals on a full-scale submerged propeller blade. A glass-fibre reinforced polymer blade has been manufactured using vacuum-assisted resin transfer moulding. During the production, 24 piezoelectric wafer sensors have been embedded into the blade. AE signals have been simulated by applying pencil lead break (PLB) excitations at several locations on the propeller blade. This has been done while the propeller was submerged in artificial seawater. For each PLB, the AE signal is measured for each connected sensor and assessed for their spectral content. The spectral content and the change in spectral content over excitation locations are used to obtain a measure of amplitude drop throughout the blade. These values can be used to assess the feasibility of measuring specific types of AE signals relating to specific types of damage mechanisms.

Regarding the organisation of the paper, firstly a description of the measurement and assessment of an AE signal is given. This includes the definition of an amplitude drop and the assumptions that are associated with that. Secondly, the experimental procedure is explained. This provides details on the manufactured propeller blade and measurement specifics. Next, results of the measurements are presented, combined with an assessment of the amplitude drop throughout the blade. Finally, conclusions are drawn and recommendations are given for future research.

2. Method

The measurement of an AE signal can be described as an AE source signal that has been distorted by wave propagation effects, sensor transfer function, and noise. For plate-like structures, the AE can propagate in the form of guided waves. These waves appear in a multitude of through-thickness deformation (wave) modes and propagate in in-plane direction. In a mathematical sense, the measurement $P(\mathbf{x}_R,\mathbf{x}_S,\omega)$ can be written as the convolution of AE source signal $\mathcal{S}_i(\mathbf{x}_S,\omega)$ with wave propagation transfer function $W_i(\mathbf{x}_R,\mathbf{x}_S,\omega)$ and sensor transfer function $D_i(\mathbf{x}_R,\omega)$, and the addition of noise $P_N(\mathbf{x}_R,\omega)$ [33, 34]. When propagating in the form of guided waves, each component can be dependent on the wave mode $i=[1..n]$ for n modes, the source location $\mathbf{x}_S$, sensor location $\mathbf{x}_R$ and frequency ω. For the source signal $\mathcal{S}_i(\mathbf{x}_S,\omega)$, multimodal contributions are captured by modal amplitude $\varsigma_i(\mathbf{x}_S)$. The frequency and phase content of the source is represented by $S(\mathbf{x}_S,\omega)$. This is elaborated in equations (2.1) and (2.2).

$$\mathcal{S}_i(\mathbf{x}_S,\omega)=\varsigma_i(\mathbf{x}_S)\,S(\mathbf{x}_S,\omega)\,. \tag{2.1}$$

$$\begin{aligned}P(\mathbf{x}_R,\mathbf{x}_S)=&\sum_{i=1}^{n}D_i(\mathbf{x}_R,\omega)\,W_i(\mathbf{x}_R,\mathbf{x}_S,\omega)\,\varsigma_i(\mathbf{x}_S)\,S(\mathbf{x}_S,\omega)\\&+P_N(\mathbf{x}_R,\omega)\,.\end{aligned} \tag{2.2}$$

Here, the wave propagation transfer function $W_i(\mathbf{x}_R,\mathbf{x}_S,\omega)$ includes attenuation, dispersion, cut-off of higher modes ($\omega_{cut,i}$) and skewing of waves as a function of location, distance and direction. Sensor transfer function $D_i(\mathbf{x}_R,\omega)$ includes electromechanical behaviour relevant to embedded piezoelectric sensors, such as the aperture effect [35, 36].

Assessment can be performed regarding the components $W_i(\mathbf{x}_R,\mathbf{x}_S,\omega)$ using measurements $P(\mathbf{x}_R,\mathbf{x}_S,\omega)$ from different known source locations to different measurement locations over the blade. Further, assessment of $P_N(\mathbf{x}_R,\omega)$ is used to examine the quality of $P(\mathbf{x}_R,\mathbf{x}_S,\omega)$.

2.1. Assessment of wave propagation

For a given sensor layout and an arbitrary source location, the drop in amplitude for specific frequency components from a sensor adjacent to the source to a sensor further away can be considered as a measure of frequency-dependent attenuation along the blade. This drop can be calculated as per equation (2.3),

$$\begin{aligned}&A(\mathbf{x}_R,\mathbf{x}_S,\omega_l)\\&\quad=\frac{P(\mathbf{x}_R,\mathbf{x}_S,\omega_l)}{P(\mathbf{x}_{Rref},\mathbf{x}_{Sref},\omega_l)}\\&\quad=\left(\sum_{i=1}^{n}D_i(\mathbf{x}_R,\omega_l)\,W_i(\mathbf{x}_R,\mathbf{x}_S,\omega_l)\,\varsigma_i(\mathbf{x}_S)\,S(\mathbf{x}_S,\omega_l)+P_N(\mathbf{x}_R,\omega_l)\right)\\&\qquad\div\left(\sum_{i=1}^{n}D_i(\mathbf{x}_{Rref},\omega_l)\,W_i(\mathbf{x}_{Rref},\mathbf{x}_{Sref},\omega_l)\,\varsigma_i(\mathbf{x}_{Sref})\,S(\mathbf{x}_{Sref},\omega_l)\right.\\&\qquad\left.+P_N(\mathbf{x}_{Rref},\omega_l)\right).\end{aligned} \tag{2.3}$$

In this equation, for each relevant frequency ω_l the amplitude drop in $\mathrm{dB}_{\mu\mathrm{V}}$ $A(\mathbf{x}_R,\mathbf{x}_S,\omega_l)$ is calculated for a sensor at location $\mathbf{x}_R$ with respect to a reference sensor at $\mathbf{x}_{Rref}$ that was adjacent to a reference source $\mathbf{x}_{Sref}$. Amplitude drop $A(\mathbf{x}_R,\mathbf{x}_S,\omega)$ can be seen as an approximation for wave propagation transfer function $W_i(\mathbf{x}_R,\mathbf{x}_S,\omega)$ (equation (2.10)). This is considered valid under five assumptions.

As a first assumption, wave propagation effects from source to reference can be regarded negligible (equation (2.4)) when the considered wave mode exists ($\omega>\omega_{cut,i}$),

$$W_i(\mathbf{x}_{Rref},\mathbf{x}_{Sref},\omega)\approx\begin{cases}0\text{ for }\omega\leqslant\omega_{cut,i}\\1\text{ for }\omega>\omega_{cut,i}\end{cases}. \tag{2.4}$$

For the second assumption, the sources of both the reference and the other signals are considered similar (equation (2.5)),

$$\varsigma_i(\mathbf{x}_S)\,S(\mathbf{x}_S,\omega_l)\approx\varsigma_i(\mathbf{x}_{Sref})\,S(\mathbf{x}_{Sref},\omega_l)\,. \tag{2.5}$$

The third assumption is that at frequency ω_l there is one dominant wave mode m. Here, the description of the wave propagation transfer functions simplify (equations (2.6) and (2.7)) and summation over wave modes $i=[1..n]$ is eliminated,

$$W_i(\mathbf{x}_{Rref},\mathbf{x}_{Sref},\omega_l)\approx\begin{cases}0\text{ for }i\neq m\\1\text{ for }i=m\end{cases}. \tag{2.6}$$

$$W_i\left(\mathbf{x}_R,\mathbf{x}_S,\omega_l\right)\approx\begin{cases}0 & \text{for } i\neq m\\ W_m\left(\mathbf{x}_R,\mathbf{x}_S,\omega_l\right) & \text{for } i=m\end{cases}. \quad (2.7)$$

The fourth assumption is that the sensor transfer function of the measurement is the same as that for the reference (equation (2.8)),

$$D_i\left(\mathbf{x}_R,\omega_l\right)\approx D_i\left(\mathbf{x}_{Rref},\omega_l\right). \quad (2.8)$$

As a fifth assumption, the noise amplitude is regarded significantly smaller than the measurement signals (equation (2.9)),

$$P_N\left(\mathbf{x}_R,\omega\right)\approx P_N\left(\mathbf{x}_{Rref},\omega\right) \ll\sum_{i=1}^{n}D_i\left(\mathbf{x}_R,\omega_l\right)W_i\left(\mathbf{x}_R,\mathbf{x}_S,\omega_l\right)\varsigma_i\left(\mathbf{x}_S\right)S\left(\mathbf{x}_S,\omega_l\right). \quad (2.9)$$

Given these assumptions, equation (2.3) is reduced to equation (2.10):

$$A\left(\mathbf{x}_R,\mathbf{x}_S,\omega_l\right)\approx\frac{D_m\left(\mathbf{x}_R,\omega_l\right)W_m\left(\mathbf{x}_R,\mathbf{x}_S,\omega_l\right)\varsigma_m\left(\mathbf{x}_S\right)S\left(\mathbf{x}_S,\omega_l\right)}{D_m\left(\mathbf{x}_{Rref},\omega_l\right)W_m\left(\mathbf{x}_{Rref},\mathbf{x}_{Sref},\omega_l\right)\varsigma_m\left(\mathbf{x}_{Sref}\right)S\left(\mathbf{x}_{Sref},\omega_l\right)} \approx W_m\left(\mathbf{x}_R,\mathbf{x}_S,\omega_l\right). \quad (2.10)$$

2.2. Assessment of noise level

The noise level can be used to define the minimum measurable signal amplitude as a reference. In the current work, the pre-trigger period $P_N^*\left(\mathbf{x}_R,\omega_l\right)$ of a measurement is regarded as an indication of the noise level. Values of $P\left(\mathbf{x}_R,\mathbf{x}_S,\omega_l\right)$ are used in the assessment when they are complying with equation (2.11), given a positive value for criterion A_N,

$$\frac{P\left(\mathbf{x}_R,\mathbf{x}_S,\omega_l\right)}{P_N^*\left(\mathbf{x}_R,\omega_l\right)}>A_N. \quad (2.11)$$

2.3. Comparison between measurement and reference AE signals

The attenuation $A\left(\mathbf{x}_R,\mathbf{x}_S,\omega_l\right)$, in conjunction with a noise level $P_N^*\left(\mathbf{x}_R,\omega_l\right)$, can then be compared to reference amplitude levels and frequency content of types of AE from literature that are associated with different damage mechanisms. This comparison gives insight in the maximum distance between AE signal source location and sensor location for different regions of the blade. This is in general relevant for the placement of embedded sensors with respect to the location and type of damage-induced AE signal to be measured.

2.4. Experimental procedure

For the experimental procedure, first the manufacturing of a composite marine propeller blade with a network of embedded piezoelectric sensors is described. This followed by a description of the experiment itself, including AE signal excitation and measurement specifics.

A glass-epoxy composite blade was produced based on the proposed geometry and stacking sequence by Maljaars *et al* [11]. The blade has a length of about 450 mm, width of 400 mm, and maximum thickness of 45 mm at the root. The production method was vacuum-assisted resin transfer moulding using a closed mould. The lay-up consists of woven fabrics at the outer layer, followed by alternately stitched unidirectional laminae and chopped strand mat (CSM) layers. In the middle of a laminate, multiple layers of CSM make up the core. In figure 1 a general overview of the manufacturing is shown. Further details on dimensions, layup and material of the blade may be found in Maljaars *et al* [11].

A total of 24 transducers were embedded at a quarter of the thickness of the blade (ply 18–25, closest to suction side). The concept and transducer distribution can be seen in figure 2. The transducers were of the PRYY + 0398 type (PIC255, Ø5 mm, t0.25 mm). The distribution pattern has been chosen such that the transducer-to-transducer distance is lower than 100 mm, as a conservative estimate (made *a priori*) for the measurement range of each transducer. Furthermore, the region near the hub has been left free of sensors in order to not create stress concentrations ([21, 37, 38]) at this generally highly loaded region. The exact locations have also been chosen to be away from ply drops in the laminate. This has been done to prevent tilting, shifting and uneven loading of the sensor during manufacturing. Wiring was through bifilar copper cables (Ø0.15 mm). Before placement into the blade, the sensors were cleaned using isopropanol to ensure proper adhesion during infusion. During lay-up of the laminae, the wiring was pulled through above laminae up to the core. Here the wiring was routed towards the hub end of the blade. After resin infusion and curing, the wires were connected to a fixture with SMA connectors. Note that for the application to the rotating propeller, this fixture is to be replaced by a slip ring or digital connection with a sufficiently high data transfer rate in the propeller hub (outside the scope of this paper).

Before and after the manufacturing, the functioning of the transducers was tested by measuring their static capacitance. In total, 22 transducers were operational. Two transducers were noted to be defective due to wiring breakage during embedding and demoulding.

The experiment involved simulation of AE signals and measurement of the propagated waves using the embedded transducers in submerged conditions. A schematic overview and the final experimental setup are shown in figure 3.

The blade was suspended into the water tank (600 × 600 × 600 mm) with blade hub and connectors of the transducers remaining above the waterline. The tank was filled with salt water (53 mS cm^{-1}, reference at 25 °C).

The excitations were based on PLBs. These are non-destructive and generate a wide-band excitation in the frequency range typical for damage-related acoustic emissions. Five locations on the blade were selected on the pressure side surface of the blade (A–E). The PLBs are denoted as red plusses in figure 2. A standard Hsu–Nielsen source was used

Figure 1. Production of a GFRP marine propeller. The left photograph shows the glass-fibre laminae inside the mould. The right photograph shows the mould under vacuum for the process of resin infusion. Photographs by W de Bles.

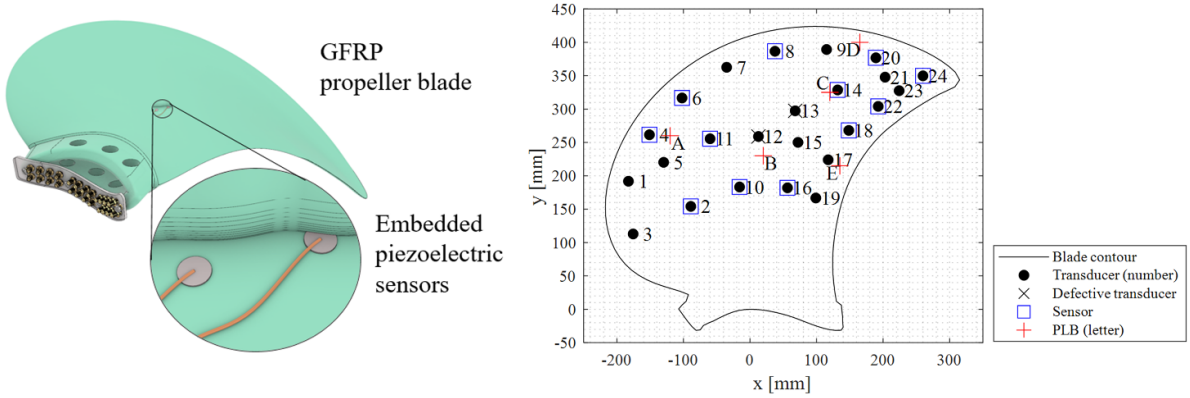

Figure 2. A GFRP marine propeller blade with embedded piezoelectric sensors: the general concept (left), and expanded view of the blade with transducer labelling and distribution (right).

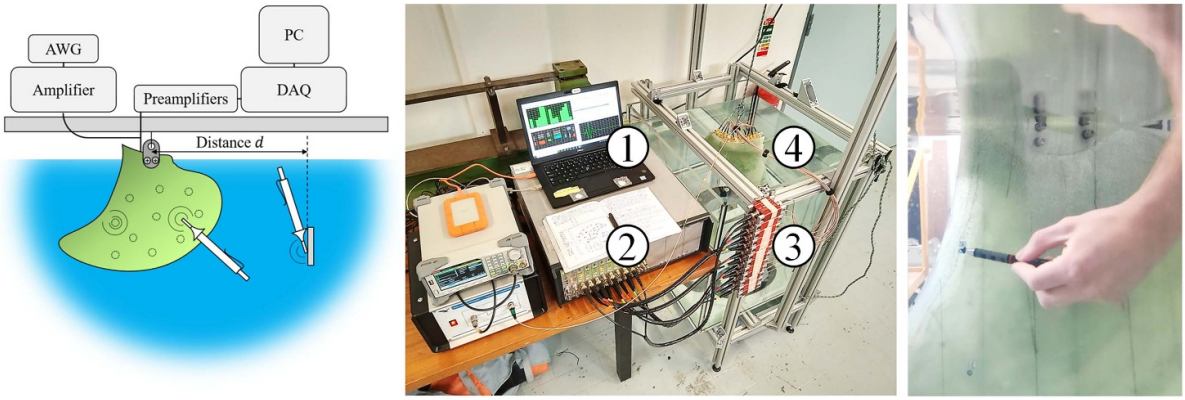

Figure 3. The experimental setup: on the left a schematic of the broader setup showing main devices and excitations (left). In the centre a photograph of the setup, where numbers 1–4 denote the measurement laptop, data acquisition system, preamplifiers and submerged propeller blade respectively. On the right photograph, the execution of an underwater pencil lead break (PLB) at position E is visible.

(Leads Ø0.35 mm, 2 H, extension 3.5 ± 1 mm). The PLBs were repeated at least five times. The PLB excitations were created by manually submerging the pencil into the water and bringing it into contact with the blade. During the excitation, motions were kept minimum to prevent additional radiated acoustic noise.

During each excitation, 12 out of 22 transducers were used (since the data acquisition system had total of 12 channels). The transducers can be seen in figure 2 as blue squares. They were connected to AEPH5 preamplifiers (40 dB), and from there to an AMSY-6 data acquisition system. The data acquisition system was grounded to the water in the tank. The data

acquisition system and preamplifiers are shown in figure 3 as parts 2 and 3 respectively. The sampling frequency was 2.5 MHz. The acquisition was hit-based and had a rearm and duration discretization time of 50 μs, and a pre-trigger period of 50 μs. A digital band-pass filter was applied ranging from 20 kHz to 850 kHz. This ensured that lower-frequency noise, such as disturbances in the water, were not measured. A detection threshold of 20 dB (with reference to 1 μV) and a floating threshold (or threshold-to-noise ratio) [39] of 6 dB were applied.

3. Results and discussion

3.1. Measurements of PLBs

The PLBs from the five locations were detected by all sensors. An example of a measurement set from PLBs in salt water is shown in figure 4. The signals are arranged from top to bottom with increasing arrival time. Note the sequence with respect to the source location.

For each of the signals, the amplitude is shown in table 1. It is noticeable that the amplitudes drop when the measurement location is further away from the source location. The measurements of sensor 4 for source location A are considered as reference measurements $P(\mathbf{x}_{Rref}, \mathbf{x}_{Sref}, \omega_l)$. This is because the high amplitudes indicate low attenuation and it is known that the distance from source to sensor is small, around 30 mm.

3.2. Drop in amplitude spectra along the blade

From the measurements described above, the drop in amplitude for specific frequency content is assessed. This follows the method of equation (2.3) described in section 2. The amplitude spectra for both the signals and pre-trigger periods are obtained through a Fast Fourier Transform. For location A, mean values of the amplitude spectra of five PLBs are given in figure 5. Note that for higher frequencies at sensors that are away from the source, values drop and approach noise levels. Furthermore, there are peaks discernable in the 100 kHz and 250 kHz region. These are visible in the measurements of $P(\mathbf{x}_{Rref}, \mathbf{x}_{Sref}, \omega_l)$, $P(\mathbf{x}_R, \mathbf{x}_S, \omega_l)$, and noise $P_N^*(\mathbf{x}_R, \mathbf{x}_S, \omega_l)$. Given its presence in both the noise and the reference measurement, these peaks are expected to be caused by the resonance frequencies of the sensors captured in the transfer function $D_i(\mathbf{x}_R, \omega)$.

Individual values from measurements are only used when compliant with equation (2.11), using an A_N of 3 dB. Mean values $\mu(P(\mathbf{x}_R, \mathbf{x}_S, \omega_l))$ are deduced from these individual measurements and used in further analysis. For a more comprehensive assessment, a moving average with a span of 10 kHz is used. Corresponding standard deviations are typically well below 5 dB.

Since reference and assessment amplitude spectra, $\mu(P(\mathbf{x}_{Rref}, \mathbf{x}_{Sref}, \omega_l))$ and $\mu(P(\mathbf{x}_R, \mathbf{x}_S, \omega_l))$, are now defined, it is possible to determine amplitude drop $\bar{P}(\mathbf{x}_R, \mathbf{x}_S, \omega_l)$ through equation (2.10). For PLB locations A–E in salt water and frequencies 100 kHz, 250 kHz and 500 kHz, contour graphs are made. These frequencies are considered to be representative of the frequencies associated with different types of failure in composite materials. The lower and mid frequency are commonly related to delamination and matrix cracking, while the mid and the higher frequency are typical for fibre breakage, respectively [23]. The contour plots are shown in figure 6. Here $\bar{P}(\mathbf{x}_R, \mathbf{x}_S, \omega_l)$ defines the isolines and colour.

From the figure, several observations can be made:

(1) Acoustic emissions are successfully measured by the embedded sensors when the blade is submerged
(2) The drop in amplitude over distance seems to be generally monotonic. This may be explained through geometrical spreading and damping effects. Interesting exceptions to this are at sources B, C and E. Here sensors along the leading edge (4,6) have relatively large values compared to sensors deeper in the blade (11,14). This is expected to be due to the lower stiffness at the edges of the blade, which can locally magnify the amplitude.
(3) For 500 kHz, there was a limitation in the distance that the amplitude drop can be quantified. This is due to the low signal-to-noise ratio at larger distances and higher frequencies. It is noticeable through the smaller domain that is covered by the sensors.
(4) For 500 kHz, attenuation is higher than for 100 kHz and 250 kHz. Besides shown in figure 6, this is also illustrated in table 2. Here, amplitude drop is normalised with the distance between source and sensor to provide an attenuation metric. Note that the values for 500 kHz are influenced by point 3.

From table 2, further it can be seen that PLB C has relatively low attenuation values. This is mainly due to the measurement at sensor 14. This sensor is close to source C, yet has a comparatively low value.

For illustration, acoustic emissions can be assessed for an indication of their maximum measurable distance $\max||\mathbf{x}_R - \mathbf{x}_S||$. Here, specific trajectories are disregarded by averaging values of $\boldsymbol{\mu}\left(\bar{\boldsymbol{P}}(\mathrm{x}_{\boldsymbol{R}}, \mathrm{x}_{\boldsymbol{S}}, \omega_l)\right) / ||\mathbf{x}_R - \mathbf{x}_S||$. Further, different values for the reference amplitude $P(\mathrm{x}_{\boldsymbol{R}ref}, \mathrm{x}_{\boldsymbol{S}ref}, \omega)$ and noise level $P_N(\mathrm{x}_{\boldsymbol{R}}, \omega)$ are considered. An A_N of 3 dB is taken into account. Values for $\max||\mathbf{x}_R - \mathbf{x}_S||$ are shown in table 3.

Table 3 illustrates that for both higher and lower frequency content and noise level, a distance of 85 mm between source and sensor typically would be sufficient. However, for a high noise level and low signal amplitude, a shorter distance would be necessitated. It should be noted that these values are indicative in nature and that a sensor lay-out can be drastically optimised. This optimisation can take place when there is specification of:

(1) The expected location and type of occurring damage
(2) The frequency content and amplitude of these damage mechanisms
(3) The expected noise level

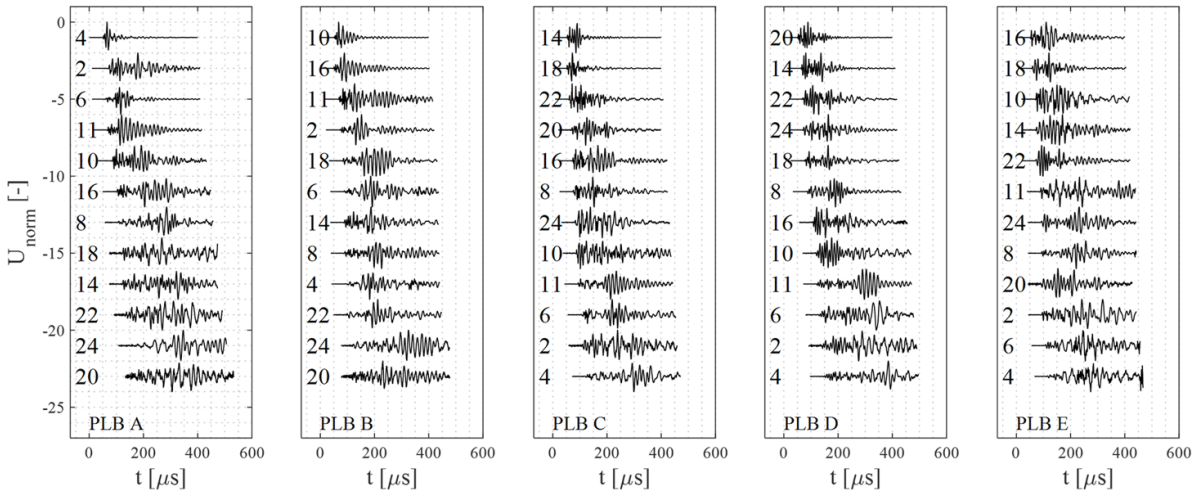

Figure 4. Measurements from a PLB at location A–E in salt water: note the general delay in arrival time and increase in dispersion from top to bottom waveform signals. The waveforms are normalised. The annotation numbers denote the sensor number.

Table 1. Amplitudes belonging to the measurements of figure 4. A grayscale is added to denote low to high amplitude values.

Sensor No.	PLB A (dB$_{\mu V}$)	PLB B (dB$_{\mu V}$)	PLB C (dB$_{\mu V}$)	PLB D (dB$_{\mu V}$)	PLB E (dB$_{\mu V}$)
2	60	68	41	41	51
4	92	62	53	54	54
6	81	60	55	53	57
8	55	58	60	66	59
10	57	86	47	47	54
11	71	63	54	56	52
14	48	56	77	70	56
16	54	77	57	51	66
18	47	60	75	64	67
20	49	53	64	81	57
22	45	55	65	66	64
24	50	49	56	68	57

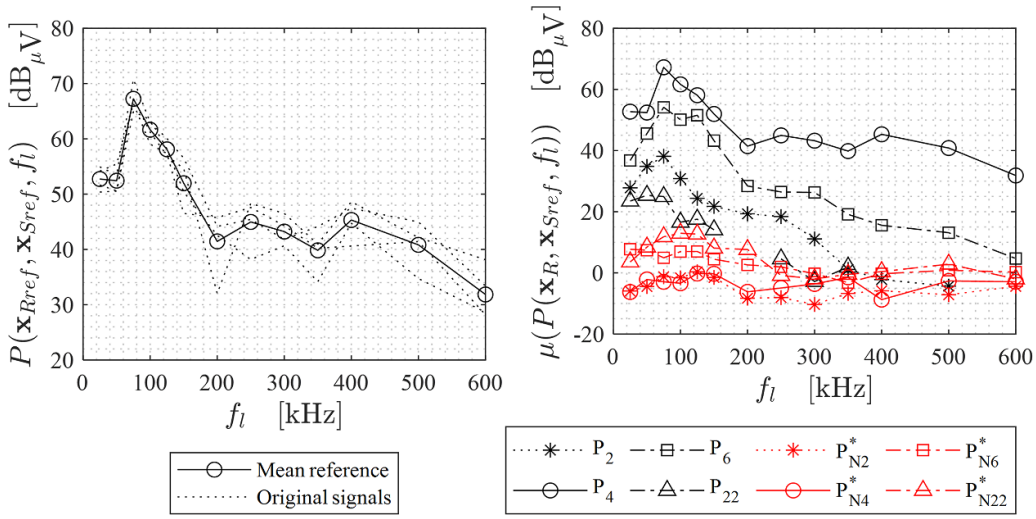

Figure 5. Amplitude spectra for measurements $\boldsymbol{P}(\mathbf{x}_{\boldsymbol{Rref}}, \mathbf{x}_{\boldsymbol{Sref}}, \omega_l)$, $\boldsymbol{P}(\mathbf{x}_{\boldsymbol{R}}, \mathbf{x}_{\boldsymbol{S}}, \omega_l)$ and noise $\boldsymbol{P}^*_{\boldsymbol{N}}(\mathbf{x}_{\boldsymbol{R}}, \mathbf{x}_{\boldsymbol{S}}, \omega_l)$. Here source $\mathbf{x}_{\boldsymbol{S}} = \mathbf{x}_{\boldsymbol{Sref}}$ is at PLB location A. The left graph shows the variation in frequency content for reference measurements $\boldsymbol{P}(\mathbf{x}_{\boldsymbol{Rref}}, \mathbf{x}_{\boldsymbol{Sref}}, \omega_l)$ and its mean. On the right graph, the mean values of $\boldsymbol{P}(\mathbf{x}_{\boldsymbol{R}}, \mathbf{x}_{\boldsymbol{S}}, \omega_l)$ and noise $\boldsymbol{P}^*_{\boldsymbol{N}}(\mathbf{x}_{\boldsymbol{R}}, \mathbf{x}_{\boldsymbol{S}}, \omega_l)$ for different measurement locations are given. Note that the subscript denotes the sensor number as per figure 2.

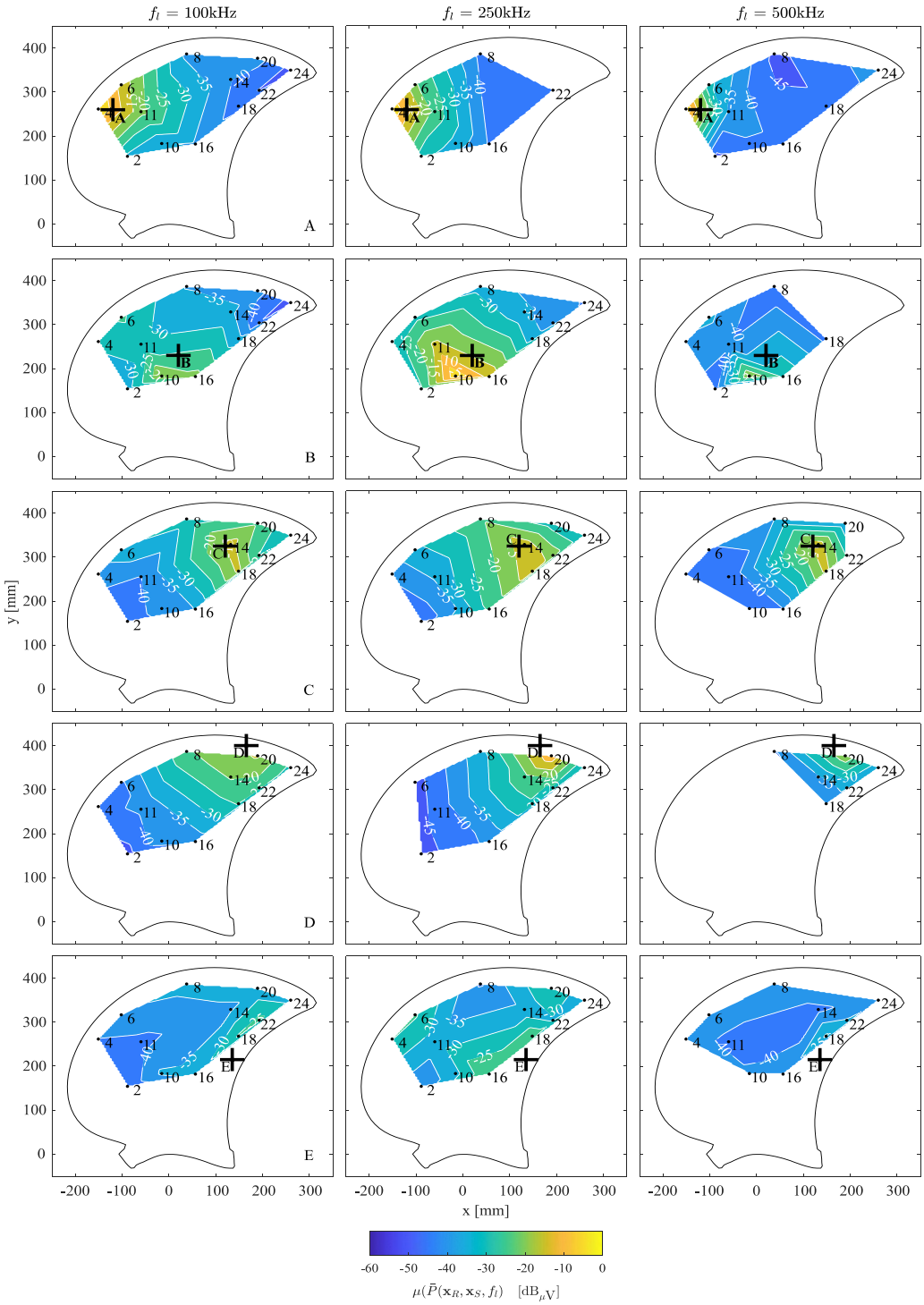

Figure 6. Mean drop in amplitude $\boldsymbol{\mu}\left(\bar{\boldsymbol{P}}(\mathbf{x}_{\boldsymbol{R}}, \mathbf{x}_{\boldsymbol{S}}, \omega_l)\right)$ for pencil lead breaks at A–E for frequency components 100 kHz, 250 kHz and 500 kHz. The location of the pencil lead break is denoted by the upright cross. Relevant sensor locations are labelled in black. The white labelling refers to the isolines.

Table 2. Attenuation $\boldsymbol{\mu}\left(\bar{\boldsymbol{P}}(\mathbf{x}_{\boldsymbol{R}}, \mathbf{x}_{\boldsymbol{S}}, \omega)\right) / ||\mathbf{x}_{\boldsymbol{R}} - \mathbf{x}_{\boldsymbol{S}}||$ averaged over sensor location in terms of dB μV mm^{-1}. A grayscale distinguishes low and high values of attenuation.

f_l (kHz)	PLB A (dB μV mm^{-1})	PLB B (dB μV mm^{-1})	PLB C (dB μV mm^{-1})	PLB D (dB μV mm^{-1})	PLB E (dB μV mm^{-1})
100	−0.18	−0.23	−0.28	−0.19	−0.23
250	−0.22	−0.18	−0.26	−0.21	−0.20
500	−0.28	−0.31	−0.33	−0.36	−0.28

Table 3. Indication of maximum measurable distance $\max||\mathbf{x}_R - \mathbf{x}_S||$ for acoustic emissions with reference amplitude $\boldsymbol{P}(\mathbf{x}_{Rref}, \mathbf{x}_{Sref}, \omega)$, noise level $\boldsymbol{P_N}(\mathbf{x}_R, \omega)$ and frequency component $\boldsymbol{f_l}$.

$P(\mathrm{x}_{Rref}, \mathrm{x}_{Sref}, \omega)$ ($\mathrm{dB}_{\mu\mathrm{V}}$)	90	70	50	90	70	50
$P_N(\mathrm{x}_R, \omega)$ ($\mathrm{dB}_{\mu\mathrm{V}}$)	20	20	20	40	40	40
$\max\|\|\mathbf{x}_R - \mathbf{x}_S\|\|$ (mm) for $f_l = (100, 250)$ kHz	307	216	124	216	124	32
$\max\|\|\mathbf{x}_R - \mathbf{x}_S\|\|$ (mm) for $f_l = 500$ kHz	215	151	87	151	87	22

The results indicate that acoustic emissions can be measured in a submerged composite marine propeller blade using embedded piezoelectric sensors. Further, typical values for amplitude drop and attenuation are given. These can in later research be used to enhance sensor locations.

4. Conclusion

For the purpose of SHM, feasibility of measuring acoustic emissions is assessed for a composite marine propeller blade. In an experimental set-up, a blade with embedded piezoelectric sensors was submerged into salt water and excited with PLBs. It was noted that:

(1) Embedded piezoelectric sensors can measure acoustic emissions on the blade when underwater.
(2) Amplitude drop has a generally monotonic behaviour over the distance from the source along the blade.
(3) There is more attenuation for higher frequency (500 kHz) components of an acoustic emission than for lower frequency components (100 kHz and 250 kHz).
(4) For typical source amplitudes and noise levels at 500 kHz frequency, a lower limit of the maximum distance between source and sensor was approximated around 87 mm. For frequencies between 100 and 250 kHz, this is 124 mm. In the case of high noise (40 dB) and low amplitude (50 dB) a shorter distance is required. It should be noted that the source-to-sensor distance can be much improved upon through anticipation of source location, type, amplitude and frequency content and noise level.

These observations highlight the feasibility of measuring acoustic emissions in composite marine propeller blades using embedded piezoelectric sensors. The presented results open up further research opportunities, such as optimisation of the sensor lay-out for different damage types, and damage localisation and characterisation methodologies for composite marine propeller blades. Moreover, these analyses can be used in conjunction with the measurement of damage-related acoustic emissions when the blade is in operation or subject to representative fatigue loading.

Data availability statement

The data cannot be made publicly available upon publication because the cost of preparing, depositing and hosting the data would be prohibitive within the terms of this research project. The data that support the findings of this study are available upon reasonable request from the authors.

Acknowledgments

This research has been performed in the context of ECoProp project sponsored by the Dutch Research Council (NWO). The authors would like to thank the project collaborators for their contribution and support. The sponsors were sparsely involved in the study design but not in the collection, analysis and interpretation of data, nor in the writing of the report. Additionally Wouter de Bles is acknowledged for his contribution to the fabrication of the test blade with embedded sensors.

ORCID iD

Arnaud Huijer https://orcid.org/0000-0003-0677-1597

References

[1] International Maritime Organization 2023 *IMO strategy on reduction of GHG emissions from ships, Resolution MEPC* 4 (International Maritime Organization) 88–100
[2] International Maritime Organization 2014 *Guidelines for the Reduction of Underwater Noise from Commercial Shipping to Address Adverse Impacts on Marine Life, MEPC.1/ Circ.833* vol 44 (International Maritime Organization)
[3] Maung P T, Prusty B G, Donough M J, Oromiehie E, Phillips A W and St John N A 2023 Automated manufacture of optimised shape-adaptive composite hydrofoils with curvilinear fibre paths for improved bend-twist performance *Mar. Struct.* **87** 103327
[4] Ng G W, Martins J R R A and Young Y L 2022 Optimizing steady and dynamic hydroelastic performance of composite foils with low-order models *Compos. Struct.* **301** 116101
[5] Hussain M, Abdel-Nasser Y, Banawan A and Ahmed Y M 2021 Effect of hydrodynamic twisting moment on design and selection of flexible composite marine propellers *Ocean Eng.* **220** 108399
[6] Choi Y S, Joe B J, Jang W S, Hong S Y, Song J H and Kwon H W 2022 Numerical investigation of BPF noise for flexible submarine propeller design including inertial force coupling *J. Mar. Sci. Technol.* **27** 648–64
[7] Young Y L, Motley M R, Barber R, Chae E J and Garg N 2016 Adaptive composite marine propulsors and turbines: progress and challenges *Appl. Mech. Rev.* **68** AMR-16-1010
[8] Shamsuddoha M, Prusty G B, Maung P T, Phillips A W and St John N A 2022 Smart monitoring of a full-scale composite hydrofoil manufactured using automated fibre placement under high cycle fatigue *Smart Mater. Struct* **31** 015025
[9] Zhang X 2021 Short-term structural performance of self-monitoring composite marine propellers *Doctoral thesis* Delft University of Technology (https://doi.org/10.4233/uuid:479b71c1-a006-4d9a-abda-b000a7711899)

[10] Van Herwerden T 2023 Fatigue Life Prediction of Composite Marine Propellers *MSc. thesis* Delft University of Technology
[11] Maljaars P, Bronswijk L, Windt J, Grasso N and Kaminski M 2018 Experimental validation of fluid-structure interaction computations of flexible composite propellers in open water conditions using BEM-FEM and RANS-FEM methods *J. Mar. Sci. Eng.* **6** 51
[12] Su Z, Pan J, Zhang S, Wu S, Yu Q and Zhang D 2022 Characterizing dynamic deformation of marine propeller blades with stroboscopic stereo digital image correlation *Mech. Syst. Signal Process.* **162** 108072
[13] Shiraishi K, Sawada Y and Arakawa D 2023 Deformed shape estimation for flexible composite marine propellers by image registration *J. Mar. Sci. Technol.* **28** 221–33
[14] Kluczyk M, Grządziela A and Batur T 2022 Design and operational diagnostics of marine propellers made of polymer materials *Pol. Marit. Res.* **29** 115–22
[15] Tian J, Croaker P, Zhang Z and Hua H 2016 Dynamic strain measurements of marine propellers under non-uniform inflow. *J. Phys.: Conf. Ser.* **744** 012094
[16] Zetterlind V E, Watkins S E and Spoltman M W 2003 Fatigue testing of a composite propeller blade using fiber-optic strain sensors *IEEE Sens. J.* **3** 393–9
[17] Seaver M, Trickey S T and Nichols J M 2006 Strain measurements from FBGs embedded in rotating composite propeller blades *Optics InfoBase Conf. Papers* (Optical Society of America (OSA)) p ThD2
[18] Javdani S, Fabian M, Carlton J S, Sun T and Grattan K T V 2016 Underwater free-vibration analysis of full-scale marine propeller using a fiber bragg grating-based sensor system *IEEE Sens. J.* **16** 946–53
[19] Ding G, Yan X, Gao X, Zhang Y and Jiang S 2022 Reconstruction of propeller deformation based on FBG sensor network *Ocean Eng.* **249** 110884
[20] Maung P T, Prusty B G, Rajan G, Li E, Phillips A W and St John N A 2017 Distributed strain measurement using fibre optics in a high performance composite hydrofoil. *ICCM Int. Confs. on Composite Materials* vol 2017 (International Committee on Composite Materials)
[21] Huijer A, Zhang X, Kassapoglou C and Pahlavan L 2022 Feasibility evaluation for development of composite propellers with embedded piezoelectric sensors *Mar. Struct.* **84** 103231
[22] Hamada R, Ogura T, Fujita S, Murayama H, Yamatogi T, Inoue T, Hayashi K, Takahara M, Goto K and Furukawa K 2023 Structural health monitoring of CFRP propellers by piezoelectric line sensors *Structural Health Monitoring S* Farhangdoust, A Guemes and F-K Chang (Stanford: DEStech Pub li ca tions, Inc. 439 North Duke Street Lan cas ter, Penn syl va nia 17602 U.S.A.) pp 408–16
[23] Saeedifar M and Zarouchas D 2020 Damage characterization of laminated composites using acoustic emission: a review *Composites B* **195** 108039
[24] Alimirzaei S, Najafabadi M A and Khodaei A 2022 Characterization of the damage mechanism of glass/epoxy composite tubes under quasi-static axial loading using acoustic emission monitoring *Appl. Compos. Mater.* **29** 1911–36
[25] Huijer A, Kassapoglou C and Pahlavan L 2021 Acoustic emission monitoring of carbon fibre reinforced composites with embedded sensors for in-situ damage identification *Sensors* **21** 6926
[26] Masmoudi S, Mahi A.E., Turki S and Guerjouma R E, 2012 Structural health monitoring of smart composite material by acoustic emission to cite this version *Structural Health Monitoring of Smart Composite Material by Acoustic Emission*
[27] Duddi M, Kocherla A and Subramaniam K V L 2024 Real-time monitoring of concrete properties using an embedded smart piezoelectric sensor with active and passive sensing abilities *RILEM Bookseries* vol 48 (Springer Science and Business Media B.V.) pp 1089–100
[28] Li W, Kong Q, Ho S C M, Lim I, Mo Y L and Song G 2016 Feasibility study of using smart aggregates as embedded acoustic emission sensors for health monitoring of concrete structures. *Smart Mater. Struct* **25** 115031
[29] Vidakovic M, Armakolas I, Sun T, Carlton J and Grattan K T V 2016 Fibre bragg grating-based acoustic sensor array for improved condition monitoring of marine lifting surfaces *J. Light. Technol.* **34** 4336–42
[30] Davies P, Dumergue N, Arhant M, Nicolas E, Paboeuf S and Mayorga P 2022 Material and structural testing to improve composite tidal turbine blade reliability *Int. Mar. Energy J.* **5** 57–65
[31] Hassan F, Mahmood A K B, Yahya N, Saboor A, Abbas M Z, Khan Z and Rimsan M 2021 State-of-the-art review on the acoustic emission source localization techniques *IEEE Access* **9** 101246–66
[32] Huijer A, Kassapoglou C and Pahlavan L 2023 Acoustic emission source localization in fiber-reinforced composites based on multimodal dispersion compensation of guided waves *Structural Health Monitoring 2023: Designing SHM for Sustainability, Maintainability, and Reliability—Proc. 14th Int. Workshop on Structural Health Monitoring* (DEStech Publications) pp 1192–9
[33] Pahlavan L, Mota M M and Blacquière G 2016 Influence of asphalt on fatigue crack monitoring in steel bridge decks using guided waves *Constr. Build. Mater.* **120** 593–604
[34] Scheeren B, Kaminski M L and Pahlavan L 2023 Acoustic emission monitoring of naturally developed damage in large-scale low-speed roller bearings *Struct. Health Monit.* **23** 360–82
[35] Monnier T, Dia S, Godin N and Zhang F 2012 Primary calibration of acoustic emission sensors by the method of reciprocity *J. Acoust. Emiss.* **30** 152–66
[36] Gopalakrishnan S, Ruzzene M and Hanagud S 2011 *Computational Techniques for Structural Health Monitoring* 1 edn (*Springer Series in Reliability Engineering*) (Springer) (https://doi.org/10.1007/978-0-85729-284-1)
[37] Chilles J S, Croxford A and Bond I P 2015 Design of an embedded sensor, for improved structural performance *Smart Mater. Struct* **24** 115014
[38] Tang H-Y, Winkelmann C, Lestari W and La Saponara V 2011 Composite structural health monitoring through use of embedded PZT sensors *J. Intell. Mater. Syst. Struct.* **22** 739–55
[39] Vallen Systeme GMBH 2020 AMSY-6 software operation manual